BIOPHYSICS

A sensorimotor instability drives a locomotor transition during fish development

Monica Coraggioso[1,2]†, Leonardo Demarchi[1,2]†, Robert Wong[3,4], Vito Dichio[5], Chloé Chaumeton[6], Thomas Panier[1,2], Ghislaine Morvan-Dubois[1,2], Geoffrey J. Goodhill[4], Volker Bormuth[1,2], Georges Debrégeas[1,2]*

Animals rely on movement to survive—to explore their environment, find food and mates, and avoid danger. During development, changes in body shape, muscle strength, and physiological needs drive the continuous adjustment of locomotor patterns. How these changes are orchestrated in a flexible and adaptive manner remains unknown. We explore this question in *Danionella cerebrum*, a miniature freshwater fish that is emerging as an important vertebrate model in systems neuroscience. We identify a clear transition in locomotion, from continuous to burst-and-coast swimming occurring around 3 weeks of age. We demonstrate that this transition is an energy-saving strategy and that it reflects an instability in the sensorimotor process governing speed regulation. Rather than a preprogrammed developmental switch, it is therefore directly tied to the animal swimming strength. We confirmed this finding by manipulating sensory feedback to induce a similar transition at fixed developmental stages. Together, our results illustrate a dynamic interplay between body, brain, and environment during development, offering insights into the principles governing adaptive locomotion.

INTRODUCTION

From birth to maturity, animal behavior adapts throughout development to accommodate changing body morphology and physiological demands. In many instances, the emergence of new behaviors is linked to brain development, driven by neuromodulatory signals or genetic programs. In mammals, for instance, hormonal signaling and transcriptional dynamics shape cortical maturation, which in turn regulates behaviors such as reproduction (*1*). In *Drosophila* larvae, neuropeptidergic signaling elicits new behaviors in preparation for metamorphosis (*2*). In zebra finches, the brain appears to rely on genetically encoded predispositions to learn song tones, even when sensory input is absent or delayed (*3*).

Locomotion—the ability to move through the environment—is the behavior most tightly linked to organismal design. It requires flexibility to accommodate morphological changes during growth (*4*) and adaptability to meet evolutionary pressures for efficient, rapid, and versatile movement (*5*). At a fixed age, transitions between locomotor modes often reflect this dynamic interplay with the environment: In humans, the walk-to-run, or in horses, the trot-to-gallop switches have been interpreted as bifurcations between locomotor attractors, whose relative stability is shaped by both biomechanics and tasks demands (*6*–*8*). Similar self-organizing principles emerge in robotics, where decentralized feedback alone can generate spontaneous gait transitions without preprogrammed rules (*9*). How new locomotor modes emerge and start being executed during development to accompany body growth remains elusive. In particular, the relative contributions of neuronal maturation and biomechanics in driving these transitions are still unclear.

Addressing this question requires a model system that permits simultaneous monitoring of behavior and brain activity throughout development. *Danionella cerebrum*, a recently established vertebrate model, offers unique advantages in this regard (*10*, *11*). Its small, transparent brain enables whole-brain calcium imaging at cellular resolution at different time points in development (*12*–*15*), while its small size and stereotyped behaviors make it amenable to detailed behavioral analysis (*16*–*18*).

In this study, we combine high-speed behavioral monitoring, fluid dynamic simulations, mathematical modeling, and virtual reality experiments to investigate how *Danionella* locomotion adapts to body growth during its early life stages, from 2 to 5 weeks post fertilization (wpf). We reveal and quantitatively characterize a developmental transition occurring around 3 wpf, during which animals shift from continuous to intermittent swimming. We assess the consequence of this transition in terms of energetic efficiency and then propose a mechanistic model to explain how intermittent swimming can spontaneously emerge. Last, we discuss the functional advantage that this mechanism offers to trigger the transition at the appropriate developmental stage.

RESULTS

High-resolution tracking reveals developmental transition in swimming behavior

To investigate how locomotor behavior changes during early development, we tracked spontaneous swimming in *Danionella* across multiple developmental stages, from larval to juvenile. A custom high-speed tracking system (Fig. 1A) was specifically engineered to minimize stress-induced behaviors, reduce wall proximity bias, and support individual-level high-throughput sampling (see also fig. S1 and Materials and Methods). While the setup captures locomotion across multiple timescales (see Fig. 1B and movies S1 and S2), here, we focus on fine-scale tail kinematics. We first quantified swimming by measuring each fish's center-of-mass velocity, v_f (Fig. 1C). This simple metric is sufficient to reveal a clear developmental transition. Up to 2 wpf, swimming is predominantly continuous with only modest

[1]Sorbonne Université, CNRS, Laboratoire Jean Perrin (LJP), F-75005 Paris, France. [2]Sorbonne Université, CNRS, Inserm, Institut de Biologie Paris-Seine (IBPS), F-75005 Paris, France. [3]Department of Electrical and Systems Engineering, Washington University in St. Louis, St. Louis, MO, USA. [4]Departments of Developmental Biology and Neuroscience, Washington University School of Medicine, St. Louis, MO, USA. [5]Laboratoire de Physique de l'ENS, PSL University and CNRS-UMR 8023, Paris, France. [6]Sorbonne Université, Institut de Biologie Paris-Seine, Paris, France.
*Corresponding author. Email: georges.debregeas@sorbonne-universite.fr
†These authors contributed equally to this work.

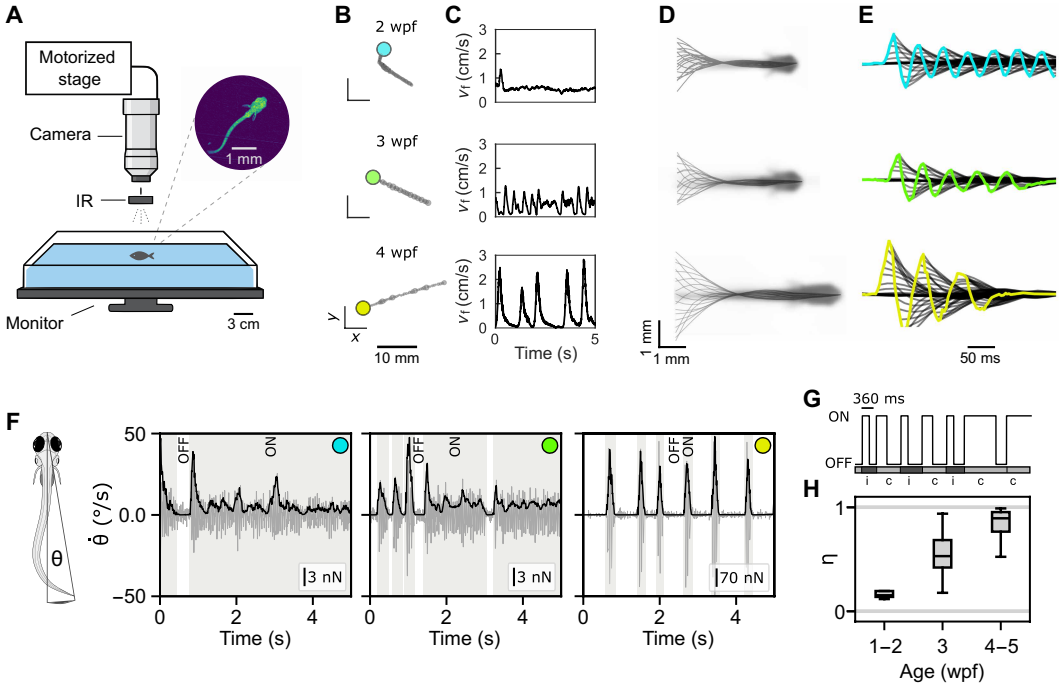

Fig. 1. Behavioral tracking reveals continuous-to-intermittent transition during early development. (**A**) Schematic of the experimental setup. A camera on a motorized stage tracks the fish at 250 FPS. Illumination is provided by infrared (IR) light-emitting diodes from above, while a monitor below the tank displays a naturalistic background (stones). Scale bar, 3 cm. An example snapshot is shown (top left). Scale bar, 1 mm. (**B**) Five-second long trajectories for three example fish of 2 wpf (cyan), 3 wpf (green), and 4 wpf (yellow). (**C**) Time evolution of center-of-mass speed v_f for the same fish. (**D**) Midline dynamics during forward motion. Time between consecutive profiles is 40 ms. The mean image of the fish across frames is shown in transparency. Scale bar, 1 mm. (**E**) Midlines are time-shifted along the *x* axis to visualize the time evolution of the tail tip (colored traces). (**F**) Schematic definition of θ, the angle between the tail tip and body axis. Its time derivative $\dot{\theta}$ (gray) is shown for three ages: 2 wpf (cyan), 3 wpf (green), and 4 wpf (yellow). The computed thrust (F_T, black) is overlaid and rescaled for comparison (scale bar in inset). F_T defines ON (gray) and OFF (white) states. (**G**) Swimming events were classified as intermittent (i) if the ON state lasted less than 360 ms, and as continuous (c) otherwise. The threshold applies only to ON-state duration; note that total event duration also includes the subsequent OFF phase. (**H**) Intermittemcy index $\eta = \frac{\#\text{ intermittent bouts}}{\#\text{ total swim event}}$ for three age groups. The median and interquartile range (IQR; 25th and 75th percentiles) are reported in the boxplot, with error bars indicating the full range of values.

speed fluctuations. By 4 to 5 wpf, fish display intermittent locomotion, characterized by bursts of propulsion separated by inactive gliding phases. This shift emerges gradually, with both patterns coexisting around 3 wpf.

We next asked whether this transition is reflected in the postural kinematics. Swimming involves axial muscle contractions that generate undulatory body waves increasing in amplitude from head to tail. Across ages (Fig. 1D), *Danionella* initiate lateral oscillations at a consistent trunk position, with a stable node located at $\sim\frac{3}{5}L$ from the head tip, where L is the fish length. This suggests that the anterior-to-posterior activation pattern is conserved. This finding is further supported by principal components analysis of segmented fish postures normalized by L. We found that the first three eigenmodes and their explained variance remaining consistent across ages (fig. S2, A to D). The characteristic tail-beat frequency also remains stable at ~20 Hz throughout development (fig. S2, F and G). Together, these observations indicate that the postural kinematics at short timescales, i.e., on the order of the tail beating period, is conserved, with the motion of older and younger fish transformable into one another through simple length rescaling.

The developmental locomotor transition is thus primarily reflected in the slower temporal modulation of the tail-beat amplitude: Tail-beating shifts from continuous oscillations to stereotypic discrete sequences of ≈3 cycles followed by periods of rest (Fig. 1E and fig. S2E).

To further characterize the emergence of burst-and-glide locomotion, we focused on the tail dynamics from which we extracted an effective thrust F_T using a fluid dynamic reactive model (see Materials and Methods). Compared to speed, F_T offers a better signal-to-noise ratio, enabling precise identification of motor activity periods: Each time point was classified as either an ON state, marked by substantial forward thrust, or an OFF state, corresponding to the absence of active movements (Fig. 1F).

Early in development, the distributions of ON and OFF state durations are broad and approximately exponential, lacking a characteristic timescale. As the fish mature, they become narrower and develop a distinct peak, revealing stereotyped burst ($\overline{\tau}_{ON} = 240 \pm 60$ ms) and pause ($\overline{\tau}_{OFF} = 430 \pm 110$ ms) durations (see fig. S3 and Supplementary Text). To quantify this evolution, the thrust signals were segmented into swimming events (or bouts) labeled "intermittent" if the ON duration was shorter than 360 ms—the mean plus two SDs of τ_{ON} in 4 to 5 wpf fish–and "continuous" otherwise (Fig. 1G). We then computed an intermittency index η defined as the fraction of intermittent events among all swimming events.

With age, η increases from $\eta \approx 0$ (continuous swimming) to $\eta \approx 1$ (intermittent swimming), as shown in Fig. 1H. Notably, while early and late developmental stages show low variability in η, values at the intermediate stage (around 3 wpf) span the full range, reflecting the heterogeneous behavior during this transition phase (fig. S4).

The locomotor transition as an energy-saving strategy

We asked whether energy saving could be a key driver behind the developmental switch in *Danionella* locomotion. Continuous swimming is expected to be more efficient at small body sizes, whereas burst-and-glide can become advantageous as fish grow larger (*19*, *20*). As body length (L) and swimming speed (v_f) increase, inertial forces begin to dominate over viscous ones. In the inertial regime, interrupting tail motion reduces drag during glides, enhancing efficiency. The relative importance of inertial and viscous forces is captured by the Reynolds number, $Re = \rho L v_f / \mu$, where ρ is the fluid density and μ its viscosity. In *Danionella*, we found that *Re* increases from 20 ± 10 to 140 ± 100 during the examined developmental window (Fig. 2, A and B), with large intra-individual variability reflecting the broad distribution of swimming speeds, particularly in older fish.

To quantitatively assess how swimming energetics evolve with development, we performed computational fluid dynamics (CFD) simulations (see Materials and Methods) (*21*). Realistic three-dimensional (3D) *Danionella* models were reconstructed from anatomical scans (see Materials and Methods and fig. S5) and animated using experimentally recorded tail kinematics (Fig. 2C and movies S3 to S6). To validate the CFD simulations, we computed the relative error between simulated and experimental speeds using an intermediate-age *Danionella*, performing both swimming modes [see Fig. 2 (E and F) and fig. S6]. This data-driven approach enables direct comparison of energetic performance between continuous and intermittent swimming, consistent with a recent large-scale computational study that systematically evaluated the hydrodynamic efficiency of burst-and-glide gaits (*22*). The simulated swimming motion generated fluid motion, which was used to compute the instantaneous dissipated power (P). Mechanical energy was obtained by integrating power over time, providing a proxy for metabolic energy cost. Efficiency was then estimated as the inverse of the energy per distance traveled.

To evaluate how swimming efficiency evolves during development, we ran CFD simulations using 3D *Danionella* models at 2 and 4 wpf, scaled to body lengths from 2.5 to 10 mm. At each size, we applied experimentally recorded tail kinematics to simulate both continuous and intermittent swimming. The resulting normalized efficiency is shown in Fig. 2 (F and G). The normalization factor, defined as the average efficiencies of continuous and intermittent swimming, enables a direct comparison between the two modes [see fig. S6 (D and E) for efficiency without normalization]. In both morphologies, simulations revealed a size-dependent shift in energetic efficiency: Continuous swimming is more efficient at smaller sizes, while burst-and-coast becomes favorable at larger sizes. The crossover occurs around 7 and 7.5 mm, slightly offset between the two 3D models, suggesting that body shape also modulates swimming efficiency. Notably, this size range (corresponding to ≈4-week-old fish) is slightly larger but close to the size at which the behavioral switch is observed, supporting the idea that burst-and-glide swimming emerges as a biomechanical adaptation to maintain energetic efficiency across development.

The velocity overshoot at the onset of movement is predictive of the bout outcome

Having established the energetic advantage of transitioning from continuous to intermittent swimming, we now ask what mechanism triggers this transition in the developing fish. Since the selection between short and long swimming events must occur within the duration of a short bout, we focus on the speed signals immediately following movement onset. Figure 3A shows bout-averaged velocity traces aligned to movement onset. Fish were grouped into three categories based on their intermittency index η: continuous ($\eta < 0.2$), mixed ($0.2 < \eta < 0.8$), and intermittent ($\eta > 0.8$). In all groups, swimming begins with one to two high-amplitude tail oscillations that lead to a peak velocity (v_{start}) reached after 100 to 150 ms. The fish speed then decays toward either a constant value or zero (see also Fig. 1E).

We found that v_{start} positively correlates with η (Spearman $r_s = 0.71$, $P = 10^{-4}$; see fig. S7). To further assess the predictive power of v_{start} on bout type outcome, we focused on the intermediate developmental stage ($0.2 < \eta < 0.8$), where both locomotor modes coexist. Swimming events were classified as either short (intermittent) or prolonged

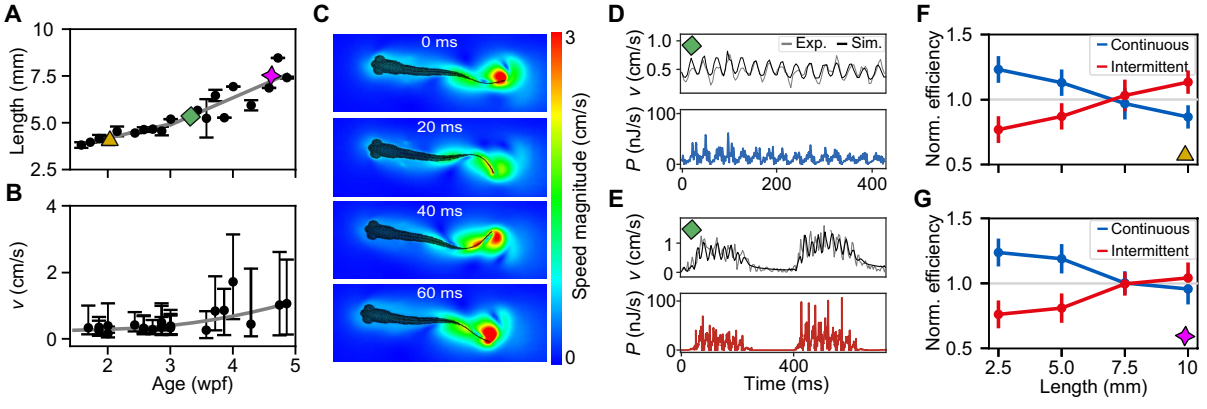

Fig. 2. Hydrodynamics of continuous versus intermittent swimming. (**A**) Fish length as a function of age (mean ± SD across individuals). Symbols indicate the three 3D model fish used for CFD simulations. Lines show linear fits before and after 3 wpf: The growth rate increases from 0.1 (≤3 wpf) to 0.2 mm/day (≥3 wpf). (**B**) Median and IQR of fish speed during active swimming across development. (**C**) Example 2D snapshots from CFD simulations, separated by 20-ms intervals. (**D** and **E**) Simulated continuous (D) and intermittent (E) swimming events using the intermediate-age 3D model. Top: Simulated (black) and experimental (gray) center-of-mass velocities. Bottom: Dissipated power (P) predicted from simulations. (**F**) Normalized efficiency versus body length using the 14 dpf Danionella morphology. Mean ± SD across simulated events for continuous (blue, $N = 11$, 11, 11, and 9) and intermittent (red, $N = 14$, 14, 14, and 11) swimming. See fig. S6E for nonnormalized data and statistical tests. (**G**) Same analysis as in (F) using the 30 dpf morphology. Continuous (blue, $N = 11$, 11, 11, and 9) and intermittent (red, $N = 14$, 14, 12, and 13) swimming. See fig. S6F for nonnormalized data and statistical tests.

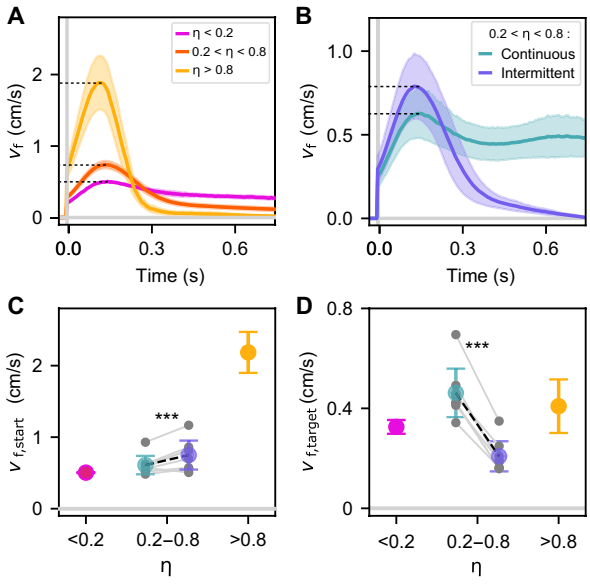

Fig. 3. Velocity overshoot at movement onset differentiates swimming modes. (**A**) Fish speed $v_f(t)$ aligned to movement onset for forward swimming events, with the subsequent 750 ms of motion shown. For each individual fish between 10^2 and 10^3, such events were recorded, depending on whether their swimming was predominantly continuous or intermittent. Fish were grouped by intermittency index η into three categories: $\eta < 0.2$ ($N = 4$), $0.2 < \eta < 0.8$ ($N = 11$), and $\eta > 0.8$ ($N = 5$). Bold lines show the mean across fish; shaded areas denote SD. (**B**) Same as in (A) but restricted to the intermediate group ($0.2 < \eta < 0.8$). Events were color-coded as continuous (cyan) or intermittent (violet) based on the bout duration criterion defined in the main text. Bold lines and shaded regions represent the group mean and SD, respectively. (**C**) Overshoot maximum speed $v_{f,start}$ as a function of η. Mean ± SD across fish are shown. In the intermediate regime ($0.2 < \eta < 0.8$), values are further separated into continuous (cyan) and intermittent (violet) events. Gray dots represent fish-specific means for each category. Two-sample *t* test: $P = 10^{-4}$. (**D**) Same as in (C) but for the average speed over time for a given swimming event, which we refer to as the target speed $v_{f,target}$ ($P = 10^{-6}$).

(continuous) using a duration threshold of ≈800 ms, defined as $\bar{\tau}_{ON}^{3wpf} + 1SD$ (Fig. 3B). The overshoot velocity v_{start} is lower in prolonged than in short bouts (Fig. 3C). This correlation was found to be statistically significant across tested fish in the intermediate regime (see Materials and Methods).

Overall, our analysis shows that the initial speed (reached within the first ~100 to 150 ms after movement onset) largely determines the ensuing swimming pattern: High initial speed generally leads to short, rapidly interrupted bouts, whereas low initial speed tends to be followed by prolonged swimming events. As a consequence, although v_{start} grows by a factor of ≈4 across the continuous-to-intermittent transition, the average bout speed over time—interpreted as an internally defined "target" speed $v_{f,target}$—increases by only ≈20 % [see Fig. 3 (C and D) and fig. S7 (B and C)].

Instability induced by sensorimotor delays drives swimming mode transition

In this section, we build on the previous observations to propose a mechanistic model that could account for the transition to intermittent swimming. Our hypothesis is that the emergence of this new locomotor mode is due to a dynamic instability of the sensorimotor system used by the animal to regulate its speed.

During continuous swimming, we observed quasi-periodic speed oscillations with a period of ≈400 ms (see fig. S9), reminiscent of those reported when *Danionella* larvae regulate their swimming speed in a virtual environment (*15*). In that context, we showed that these oscillations arise from a finite delay (≈100 ms) in the visuomotor feedback loop. This suggests that *Danionella* rely on sensory feedback for speed regulation even during freely swimming and that similar delays influence this control. Such a mechanism can also explain the velocity overshoot at bout onset (Fig. 3, A and B): The initial high velocity period likely reflects a ballistic phase (no feedback) lasting for ≈100 ms, followed by deceleration as sensorimotor regulation engages to drive the system toward a target speed.

The sensorimotor loop is schematized in Fig. 4A. We assume that the fish can estimate its speed v_f (the way it does so will be discussed in the next section) and adjusts its motor command u based on the difference between v_f and an internally defined target speed $v_{f,target}$. This motor command drives the tail oscillation speed v_t, which in turn sets v_f. The loop can be mathematically described by a system of three linear equations

$$\frac{du}{dt} = -k_u\left[v_f\left(t-\tau_u\right) - v_{f,target}\right] \quad (1)$$

$$v_t(t) = k_t u\left(t-\tau_t\right) \quad (2)$$

$$v_f(t) = k_f v_t\left(t-\tau_f\right) \quad (3)$$

where v_t is the tail-tip speed averaged over one oscillation cycle: $v_t = 2Af$, with A the peak-to-peak amplitude and f the (invariant) tail-beat frequency. The motor command u denotes an upstream neuronal signal driving the tail amplitude. Each step in the sensorimotor loop has an associated gain (k_u, k_t, and k_f) and delay (τ_u, τ_t, and τ_f). Although sensory and motor signals are likely encoded nonlinearly in sensorimotor circuits (*15*), here, we assume linear relationships in Eqs. 1 and 2 for interpretability; however, we show in section S1.3 that including logarithmic nonlinearities yield analogous conclusions.

Equation 3 describes how tail motion determines the fish's forward swimming speed. The proportionality constant k_f can be expressed in terms of the Strouhal number $St = Af/v_f$ as $k_f = 1/(2St)$. Consistent with literature (*23*), we found that St slowly decreases with *Re*, resulting in a small increase of k_f across the probed developmental window (see fig. S10). Regarding the delay τ_f, we found it to be approximately invariant. It should be noted however that the sharp delay used in Eq. 3 is a simplifying approximation as an exponential kernel provides a better match between tail and fish speed.

We can obtain a differential equation for each of the three variables (v_t, v_f, and u) by expressing any pair of them using Eqs. 2 and 3 and substituting them into Eq. 1. The resulting equations have the same form and can therefore be written generically for a variable V as

$$\frac{dV}{dt} = -K\left[V(t-\tau) - V_{target}\right] \quad (4)$$

where τ is the sum of the delays of the sensorimotor loop, $\tau = \tau_u + \tau_t + \tau_f$, whereas the gain K corresponds to the product of the various gains, $K = k_u k_t k_f$. Equation 4 is a linear delayed feedback equation which can be solved analytically (*15*). Its behavior depends on the sole

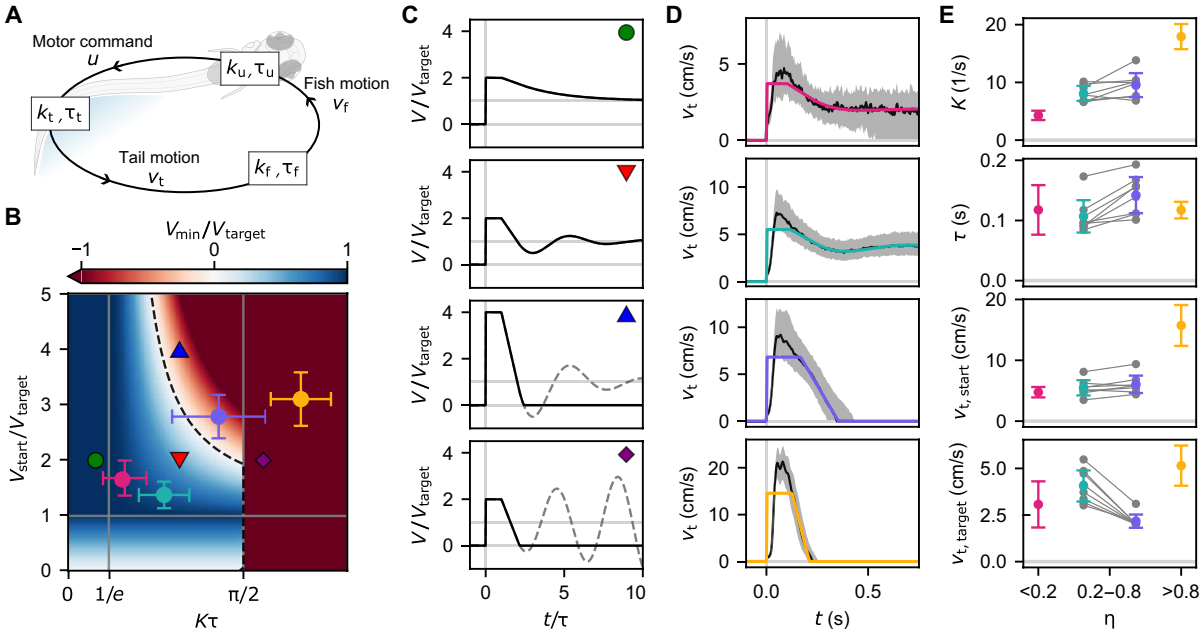

Fig. 4. A model with delayed feedback control reproduces the locomotor transition. (**A**) Schematic representation of the sensorimotor loop for speed regulation. (**B**) Minimum speed V_{min}, defined as the lowest value reached during the first oscillation of a speed transient evolving according to Eq. 4, as a function of the onset speed V_{start} and gain delay product $K\tau$ (see eq. S3). All speeds are normalized by the target speed V_{target}. The gray vertical solid lines delineate the different dynamic regimes of the linear model. The black dashed line corresponds to $V_{min} = 0$ and separates the regions of continuous (blue) and intermittent (red) swimming. (**C**) Example traces showing the evolution of the speed according to Eq. 4 for different values of the parameters [corresponding symbols in (B)]. If the speed reaches zero, swimming stops (black solid line), although the mathematical solution would continue to oscillate (gray dashed line). (**D**) Fitting the onset profiles of tail speed $v_t(t)$ (black solid lines: median; gray shaded areas: IQR) using the analytical solutions of Eq. 4 (colored solid lines; see eq. S2). Fits are shown for three representative fish, using the same classification and color code as in Fig. 3 (A and B). (**E**) Best fit values of the parameters shown for different fish (error bars indicate mean and SD), separated in four groups as in Fig. 3C. These values were used to compute the corresponding error bars in (B). The values corresponding to individual fish are shown as gray points for 3 wpf fish.

dimensionless parameter $K\tau$ (see section S1.2). For $K\tau < 1/e$, the solution converges exponentially to V_{target}, for $1/e < K\tau < \pi/2$, it converges to the same value through damped oscillations, while for $K\tau > \pi/2$, the system is unstable and displays diverging oscillations (Fig. 4, B and C). Assume a fish starts swimming with an initial speed V_{start}. After a time τ, it begins regulating its speed toward the target value V_{target}. Depending on the gain-delay product $K\tau$ and the ratio V_{start}/V_{target}, the speed may either converge to the target value—possibly with damped oscillations—or it can reach a negative minimum value V_{min} (Fig. 4C). Since negative speeds are physiologically impossible, the fish effectively halts, resulting in the execution of a short bout. This bifurcation, inherent to the delay differential equation that governs sensorimotor regulation (Eq. 4), thus offers a simple mechanism for the observed locomotor transition.

We sought to infer the model parameter values for fish at various developmental stages. To this end, we fitted the evolution of the tail speed at the onset of swimming using eq. S2 (see Materials and Methods). For fish in the intermediate stage ($0.2 < \eta < 0.8$), we separately considered the short and prolonged bouts as in Fig. 3B. The model reproduces the observed velocity decay across conditions, preceded by an initial period τ during which we assume constant v_t (Fig. 4D). The initial and target tail speeds $v_{t,start/target}$ estimated from the fit (Fig. 4E) follow the same trends as those obtained from the measured fish speed in Fig. 3 (C and D). The inferred sensorimotor delay τ remains stable across fish and ages, while the gain K increases ≈4-fold with development. When represented in the dynamic phase space, we find that, as fish grow, the system moves into the unstable region (Fig. 4B). Variability in swimming mode at the intermediate stage appears to be largely explained by differences in initial and target speeds: Higher $v_{t,start}/v_{t,target}$ ratios lead to short bouts, lower ones to continuous swimming.

As τ is approximately constant and $v_{t,target}$ varies weakly across development (see Fig. 4E), the transition to instability can be primarily attributed to the growth in K and $v_{t,start}$. We recall that the sensorimotor gain $K = k_u k_t k_f$ encompasses the three successive transformations of the sensorimotor loop. We therefore examine the evolution of each of these three gains. The internal gain k_u is unknown, but within the scope of our model, we hypothesize that the transition is controlled by physiological rather than neuronal factors and thus assume that k_u (and the initial motor command u_{start}) remains constant across development. As mentioned earlier, k_f shows only a modest increase during development (fig. S10C), which cannot account for the observed fourfold rise in K. The transition is therefore mainly driven by k_t, which sets the relationship between motor command and tail speed. This parameter is expected to increase as the fish grows and progressively develops more strength and greater thrust (*24*), driving a concurrent increase in the initial speed $v_{t,start} = k_t u_{start}$.

We conclude that, while maintaining the motor control mechanism for speed regulation unchanged, the sole strengthening of the fish during development can drive the system across the bifurcation threshold, corresponding to a transition from continuous to intermittent swimming.

Transition between continuous and intermittent swimming can be externally induced

Our mechanistic model implies that *Danionella* can internally estimate self-motion—with a short delay—to gauge its own speed v_f and achieve a target speed $v_{f,target}$. Self-motion estimation is a complex and distributed multisensory process that remains challenging to dissect. Here, we aim to identify which sensory modality dominates in freely swimming fish and then test the model by manipulating sensory feedback to assess its impact on the swimming mode selection.

We ran experiments in which we successively altered the visual, lateral line, and vestibular feedback in freely swimming animals. We found that locomotor behavior was largely unaffected in fish swimming in complete darkness or after lateral line ablation (see Materials and Methods and fig. S11), indicating that neither vision nor the lateral line system serves as the primary input for self-motion estimation. To externally manipulate vestibular input, we placed 5 wpf *Danionella* in dextran solution with a viscosity 10 times higher than that of water (see Materials and Methods). We observed that the fish, which at this age swim intermittently in water, now reversed to continuous swimming as shown by the large increase in the swim event duration (Fig. 5B and movie S7). This observation is consistent with the model prediction under the assumption that velocity estimation relies primarily on vestibular input. The increase in medium viscosity leads to an effective reduction of the coefficient k_f that controls the relationship between the fish speed and the tail motion, as evidenced by the ≈3-fold reduction of the onset speed $v_{f,start}$ (Fig. 5A). As a consequence, the system is expected to cross back over the bifurcation line and settle in the continuous regime of the phase space, corresponding to low $K\tau$ and low $v_{f,start}/v_{f,target}$ (see Fig. 4B).

We wondered whether this effect is a specific by-product of altered vestibular input, or whether it more generally reflects the system response to changes in the sensorimotor loop. To this end, we performed experiments in head-tethered animals (Fig. 5C), in which vestibular feedback is absent, using the same virtual reality setup as in Demarchi *et al.* (*15*) (see Materials and Methods). In this configuration, the fish relies on optic flow to regulate its speed and stabilize position in response to externally imposed visual currents, a behavior known as the optomotor response (OMR). While in the freely swimming configuration, the target speed is set internally, here, we can externally define $v_{t,target}$ and probe its effect on the swimming regime (see also Supplementary Text and fig. S12). In 2 wpf fish, lowering the target speed triggered a shift from continuous to intermittent swimming (Fig. 5D, left). Conversely, we found that 4 wpf fish could switch to continuous swimming for high enough target speed (Fig. 5D, right). Thus, for both ages, bout duration increased with target speed (Fig. 5E; see also fig. S4B for bout durations in freely swimming fish). Together, these results show that *Danionella* can engage in either swimming modality at any developmental stage and that the selected swimming pattern depends on the sensorimotor system and can be externally controlled.

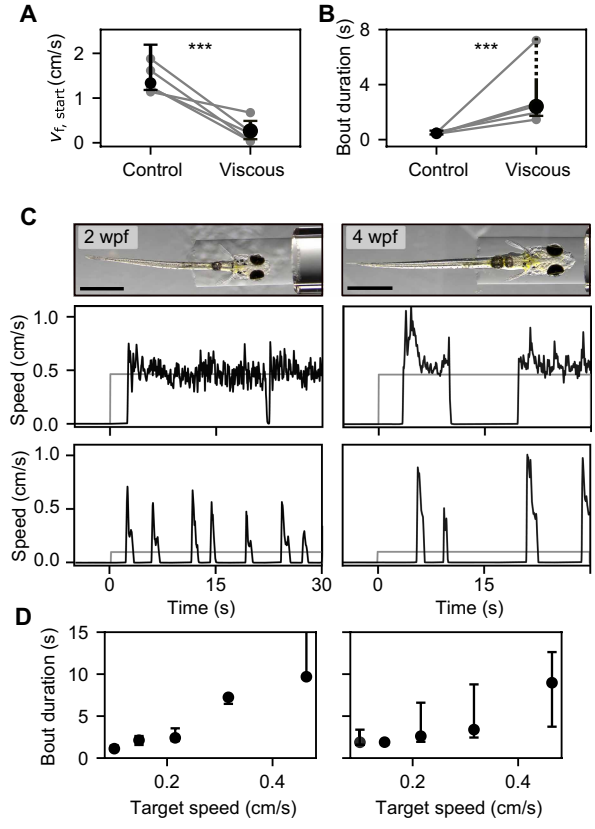

Fig. 5. Locomotor transition can be externally induced. Comparison of swimming kinematics in water (control) and viscous medium. (**A**) $v_{f,start}$ (median ± IQR) across fish ($N = 5$); gray lines show average values of different swimming events for individual fish. Mann-Whitney U test: $P = 10^{-4}$. (**B**) Bout duration (median ± IQR) across fish. In viscous media, fish typically swam until reaching the end of the—smaller—experimental tank (see Materials and Methods), making the upper bound of bout duration not meaningful. Mann-Whitney U test: $P = 10^{-4}$. (**C**) Top: head-fixed fish at 2 and 4 wpf, prepared for virtual reality experiments. Scale bars, 1 mm. Bottom: example traces of fish fictive velocity (black) in response to forward visual motion for two target speeds (shown in gray). (**D**) Bout duration (median ± IQR) versus target speed in 2 wpf (left, $N = 5$) and 4 wpf (right, $N = 5$) fish ($N = 5$ each).

DISCUSSION

By systematically monitoring the maturation of locomotor behavior during early development in *D. cerebrum*, we identified a transition from continuous to burst-and-glide swimming that occurs at around 3 weeks of age. We observed that the acceleration at the onset of movement is predictive of the ensuing swimming modality: High initial acceleration tends to be followed by a sharp deceleration and the interruption of movement, whereas low acceleration is likely to initiate a prolonged swimming period. This nontrivial correlation supports a mechanistic model of sensory-regulated swimming in which the locomotor transition naturally emerges as a dynamic instability of the delay sensorimotor loop through which the animal regulates its speed.

The model accounts for the observation that fish in the intermediate regime can exhibit both swimming modes, as they can initiate movements with acceleration above or below the threshold of instability. It also explains why intermittently swimming fish placed in a viscous fluid revert to continuous navigation. Within the scope of this model, the locomotor modality is determined by the hydrodynamic regime rather than by chronological age.

The sensorimotor feedback loop underlying the locomotor instability requires self-motion estimation. To compute this estimate, animals may use visual, proprioceptive, mechanosensory, motor efference copy, and vestibular inputs. Our experiments show that

freely swimming *Danionella* primarily estimate their own speed by integrating vestibular signals at movement onset. However, on a longer timescale, this estimated velocity will accumulate errors, so we expect other sensory modalities to contribute to speed regulation, as observed in mice (*25*) and *Drosophila* (*26*). This is also the case when vestibular feedback is unavailable, as in head-tethered configurations, for which *Danionella* rely on optic flow to regulate their speed.

Our hydrodynamic simulations showed that the continuous-to-intermittent transition enables the fish to minimize energy expenditure across development. Consistent with previous studies (*19*, *20*, *22*, *27*, *28*), burst-and-glide swimming becomes energetically favorable as inertial forces become more important during growth. On the basis of energetics alone, one would however expect the transition to occur at 4 rather than 3 weeks of age. This small discrepancy in the transition timing could reflect the fact that energetics alone cannot fully explain the complex ecological and evolutionary adaptations of aquatic organisms across body sizes. For instance, oxygenation or self-generated sensory noise may depend on the swimming mode and could also play a role in determining the optimal swimming strategy (*29*, *30*). Furthermore, our simulations exclusively account for tail motion, without incorporating the contribution of pectoral fin movements.

The proposed mechanism offers a simple, adaptive, and flexible control strategy to trigger locomotor transition. In our model, the internal sensorimotor parameters (notably k_u and u_{start}) are evolutionarily tuned so that the transition is triggered when intermittent swimming becomes energetically beneficial. Once these parameters are set, the switch becomes solely dependent on the fish physiology through the thrust that the animal can develop and not tied to a rigid developmental program. This mechanism ensures that the transition timing is robust against the large variability in body growth observed in natural conditions due to, e.g., differences in rearing temperatures (*31*) or sexual specialization (*32*).

This control strategy is parsimonious: Our model shows that an explicitly programmed neural "switch" is not required to explain the transition. However, it does not rule out the possibility that the motor command (denoted u in our framework) varies across development and therefore contributes to the observed locomotor transition. Definitive confirmation or exclusion of this possibility would require functional recording of the involved sensorimotor circuits across developmental stages.

In this simplified modeling framework, the motor output signal is reduced to a single parameter that controls the amplitude of tail oscillations. This parameter should therefore correspond to the activity of an upstream circuit regulating tail-beat amplitude. In zebrafish, the medial longitudinal fasciculus has been identified as a key higher-order center to control the animal forward speed (*33*, *34*). In *Danionella* larvae, this midbrain neuronal population has been shown to similarly correlate with the animal swimming speed (*14*, *15*, *29*), making it a natural candidate to encode the output signal of the sensorimotor process.

We note that a similar transition from continuous to intermittent swimming has been reported in anchovy larvae by Weihs in the late 70s and was likewise interpreted as an energy-saving strategy (*35*). Moreover, several teleost larvae appear to exhibit less stereotyped swimming patterns compared to the burst-and-glide mode. This seems to be the case for medaka larvae (*36*), as well as during prey-capture behaviors across four different cichlid species (*37*). However, thrust generation was not formally quantified during development in these studies. Given the morphological and ecological proximity between larval zebrafish and *Danionella*, one might expect similar mechanisms to be at play in zebrafish as well. Yet, from the onset of motility, zebrafish swim intermittently, and unlike *Danionella*, we were unable to induce a switch to continuous swimming by altering medium viscosity (fig. S13). Similarly, during OMR assays, zebrafish consistently swam intermittently, regardless of the visual target speed (*33*, *38*, *39*). In *Danionella*, continuous swimming is restricted to a relatively short developmental window (1 to 3 weeks), during which body length increases by less than 20% (growth rate ≈ 0.1 mm/day; fig. S13A), whereas zebrafish exhibit steady and more rapid growth up to the juvenile stage (growth rate ≈ 0.2 mm/day; fig. S13A). On the basis of on how efficiency scales with size for the two swimming modes (Fig. 2F), one would expect zebrafish to also exhibit an initial phase of continuous swimming, although shorter than that observed in *Danionella*. Other constraints, beyond energetics, may have evolutionary driven the complete elimination of this locomotor pattern. The impossibility to induce continuous swimming through sensory manipulation in zebrafish actually suggests that intermittent motion is hardwired in this animal. These behavioral differences point to potential species-specific solutions to the form-function optimization problem, opening avenues for cross-species comparative studies. Extending to artificial systems, the sensorimotor adaptive mechanism we propose could inspire the design of self-adjusting robots capable of switching between swimming modes based on global parameters to optimize efficiency (*40*).

MATERIALS AND METHODS

Fish care

All experimental procedures involving fish (*D. cerebrum*) were approved by the ethics committee "Le Comité d'Éthique pour l'Expérimentation Animale Charles Darwin C2EA-005" (APAFIS authorization number: 52420-2024121210531432 v7). Fish are housed in the facility, with water temperature maintained at approximately 27°C, pH at ~7.3, and conductivity around 330 μm. The room lighting followed a 14/10-hour day/night cycle.

Tanks were monitored daily to collect newly laid egg clutches, which were transferred to petri dishes containing E3 medium and kept at 28°C in an incubator. After hatching, larvae were transferred to 1-liter beakers and fed with rotifers twice a day until 2 weeks of age (±1 day), after which they were either used for experiments or transferred to 3-liter tanks in the main water flow system. Adult fish were maintained in a recirculating water system, housed in groups of approximately 50 individuals in tanks with a volume of 30 liters.

All the experiments were conducted using wild-type animals. Animals were transferred from the fish facility to the experimental room 1 day before the planned experiments. All experiments were performed between 10:00 a.m. and 5:00 p.m. Fish were euthanized immediately following the conclusion of the experiments.

Swimming assay design

Arena design

Individual fish swam freely in a large arena (40 cm–by–40 cm, approximately 100× the fish body length), filled with filtered system water to a depth of 1 cm. This open-field configuration allowed for spontaneous swimming while minimizing wall effects and promoting naturalistic exploratory behavior (see schematic in Fig. 1A and photographs in fig. S1).

Camera system

A high-speed camera (PointGrey FlyCapture), mounted on a motorized XY stage, followed the fish in real time and recorded images at 250 frames per second (FPS). Infrared illumination was provided via a custom optical path consisting of an infrared light-emitting diode and a beamsplitter (Thorlabs), ensuring homogeneous lighting without interfering with the animal's behavior. To maintain consistent spatial resolution across *Danionella* developmental stages, the camera field of view was adjusted to preserve a constant 1:4 ratio between fish body length and field of view size.

Motorized stage

The camera and light source were mounted on a 3D printer machine (Shapeoko 4, Carbide3D), repurposed for live tracking. Motor control was implemented via an open serial API using G-code commands, enabling full customization of the motor's speed and position based on the fish's real-time speed and position. Motor response time was ~50 ms.

Real-time tracking

The real-time fish position was estimated using a weighted average $\mathbf{x}_f(t) = (1-\eta)\ \mathbf{x}_{cv} + \eta\ \mathbf{x}_{AI}$, where $\mathbf{x}_{cv}$ is the position computed using a classic computer vision algorithm (background subtraction, binarization, and centroid detection), which is fast but susceptible to noise. In contrast, $\mathbf{x}_{AI}$ corresponds to the position estimated by an artificial intelligence (AI)–based object detection pipeline, implemented using YOLOv5 (*41*) and trained on a curated dataset of annotated *Danionella* images. While more accurate, the AI model required careful optimization to meet real-time processing constraints. Its confidence score η dynamically weighted the two estimates. No predictive model was required: the tracking system operated with a latency of ~20 ms, which was sufficient to reliably follow the fish in real time.

Experiment duration and data handling

Each session lasted up to 2 hours per fish. In the case of tracking loss, the camera was manually recentered on the fish, and the experiment resumed as a new "run." Multiple runs per fish were pooled during analysis. Raw video data were saved for downstream processing (see the "Pose estimation and kinematic extraction" section).

System implementation

Experiments were conducted under controlled environmental conditions: constant illumination and stable water temperature (26°C), maintained by a custom wooden enclosure surrounding the setup. To minimize disturbances, visual stimuli were reduced by shielding the motorized stage with a dark infrared filter (Goodfellow), and mechanical vibrations were dampened by physically decoupling the motorized stage from the arena.

The setup was inspired by Johnson *et al.* (*42*), with several improvements to increase spatiotemporal resolution and tracking robustness. Camera acquisition, motor control, and real-time tracking were handled via parallel threads using Python's built-in threading module, ensuring low-latency communication and synchronization across components. Hardware and software were fully customized for these experiments, and all programming was performed in Python.

Pose estimation and kinematic extraction

The pose of the animal was extracted from raw video recordings using a custom Python-based workflow. Initially, we applied SLEAP pose tracking (*43*) to detect five key points along fish body while also identifying and discarding low-confidence frames based on the model's confidence scores. To further refine positional accuracy, each frame was registered using a reference image of the head to correct for residual rigid body transformations. Last, the midline of the fish was segmented in 20 equispaced points using the Stytra algorithm (*44*). Since postures are measured in 2D projection, the body length varies slightly across frames due to changes in animal pitch angle; therefore, in Fig. 2A, L is reported as mean ± SD rather than a fixed value.

All video-derived measurements are transformed into the laboratory frame of reference by appropriately combining them with the motor position recorded during the experiment. The instantaneous speed of the fish is given by $v_f(t) = \sqrt{\left(\delta x(t)^2 + \delta y(t)^2\right)}/dt$, prior Savgol filtering of $x(t)$ and $y(t)$ in a time window of 60 ms to filter out undulations of the body center of mass.

The speed of the tail is defined as $v_t(t) = L\dot{\theta}(t)$, where L is the fish length and θ is the angle formed between the tip of the tail and the fish midline. In particular, we compute $v_t(t) = L\mathrm{H}\left[\dot{\theta}(t)\right]$, where $\mathrm{H}\left[\dot{\theta}(t)\right]$ is the Hilbert transform of $\dot{\theta}(t)$, used to extract its envelop.

Reactive model for thrust estimation

To estimate the thrust from the tail movements, we followed an approach that was used in previous studies on undulatory locomotion at intermediate Reynolds numbers (*45*). We define a curvilinear coordinate system along the tail, with s going from 0 at the tip of the head to l at the tip of the tail. If $\vec{v}_t(s)$ is the speed of the tail element at position s and $\hat{n}_\perp(s)$ the unit vector perpendicular to the local tail segment, then $v_\perp(s) = \vec{v}_t(s) \cdot \hat{n}_\perp(s)$ is the component of the speed perpendicular to the tail itself. Then, the reactive force on a tail segment of length ds at position s along the tail is given by

$$d\vec{F}_T(s) = -\frac{1}{2}\rho c_d v_\perp^2(s)\hat{n}_\perp(s)h\,ds \tag{5}$$

where c_d is the drag coefficient, ρ is the water density, and h is the height of the tail segment. Then, if the fish heading direction is along $\hat{n}_{fish}$, then the instantaneous thrust resulting from the motion of the segment is given by the component along the direction of motion $dF_T(s) = d\vec{F}_T(s) \cdot \hat{n}_{fish}$. We get the total average thrust by integrating over the whole tail and averaging over one tail-beat period

$$F_T = -\frac{1}{2}\rho c_d h\left\langle \int_0^l v_\perp^2(s)\hat{n}_\perp(s)\cdot\hat{n}_{fish}\,ds \right\rangle_{\text{tail-beat period}} \tag{6}$$

To compute F_T, we considered an approximately constant tail height $h \approx 0.7$ mm and drag coefficient $c_d \approx 1$. Using F_T, we defined ON and OFF states by setting a threshold that maximally separates active tail movements from background noise.

CFD simulations

The CFD simulations were adapted from previous immersed boundary frameworks (*21*, *46*). At each time step, experimentally recorded midline kinematics were mapped onto a 3D fish surface model to generate time-resolved surface velocities. Relative xy displacements of each midline point were used to drive the motion of corresponding transverse slices of the 3D mesh. Velocity mapping and preprocessing were implemented using the Eigen C++ library (*47*).

Simulations were run in IBAMR (v0.15.0 and v0.16.0) with native MPI support for parallel computation. A domain-refined adaptive

grid was used, and simulation parameters (e.g., viscosity and density) matched experimental estimates. Validation followed previous approaches (*21*), comparing CFD-predicted speed at the swim bladder with experimental measurements.

Energy was calculated as mechanical power output integrated over time, and efficiency was defined as distance traveled per unit energy. To compare swimming styles, we used tail kinematics recorded from 13 and 34 days post fertilization (dpf) *Danionella* as representative examples of the two extreme phenotypes: continuous and intermittent swimming, respectively. These kinematics were applied to animate 3D model fish at 14 and 30 dpf, rescaled to four different body lengths (2.5, 5, 7.5, and 10 mm). The rationale was not only to test the effect of body length on swimming energetics in the two swimming modes but also to assess the contribution of morphological changes in body shape between 2 and 5 weeks. Simulation results were visualized and postprocessed using VisIt (*48*).

3D fish models

3D fish models were obtained from lightsheet-based 3D stacks of clarified specimen, using the CUBIC-R+(N) clearing protocol from (*49*). After fixation and fluorescein fluorescence staining, samples were embedded in low gelling temperature agarose (2%; A9414, Sigma-Aldrich). They were then incubated in 2 ml of 50% CUBIC-R+(N) reagent, composed of 45% (w/w) antipyrine (A5882, Sigma-Aldrich), 30% (w/w) nicotinamide (A15970, Thermo Fisher Scientific), and 0.5% (w/w) *N*-butyldiethanolamine (471240, Sigma-Aldrich), diluted in MilliQ water. Incubation was performed for 1 day at room temperature, followed by 1 day in 2 ml of 100% CUBIC-R+(N). Specimen was then transferred in fresh CUBIC-R+(N) reagent inside the imaging tank and left for a few minutes to allow refractive index homogenization.

Lightsheet imaging was performed with the Alpha3 system (see Table 1), equipped with a 10× XL Plan N objective (XLPLN10XSVMP, Olympus, Japan) with a refractive index adaptive collar (1.33 to 1.52) and a scientific CMOS Orca Flash4 camera (Hamamatsu, Japan). The acquisition software QtSPIM (version 2.20) was used. A 488-nm excitation laser and the ET525/50m emission filter were used for imaging. Lightsheet images were converted using arivis SIS Converter 3.1.1 and analyzed with arivis Vision4D 3.0.1 software (arivis AG, Germany).

Correlation between onset initial speed and bout duration

To quantify the correlation between the onset initial speed v_{start} and the swimming event duration, we computed receiver operating characteristic (ROC) curves for all intermediate-stage fish (fig. S8). For all but two animals, the ROC deviated significantly from chance (z-score $> 3\sigma$), with a mean area under the curve $AUC_{ROC} = 0.63 \pm 0.08$, indicating moderate but notable predictive accuracy.

Table 1. Optical configuration of the lightsheet imaging system. Imaging was performed with the 488-nm laser. NA, numerical aperture; RI, refractive index.

System	Type	Objective (NA)	Lasers
Lightsheet Alpha3 (PhaseView, France)	Lightsheet	XLPLN 10× Olympus objective (0.6 NA), multi-immersion collar (RI 1.33 to 1.52)	405, **488**, 561, and 635 nm

Fitting onsets with delay equation

For each fish, we considered the onset speed signal averaged over all swimming events. We focused on the tail speed signal v_t as we expect it to more closely reflect the dynamics of the underlying motor command. For the parametric model used in the fit, we considered the analytical solution of Eq. 4 for a constant initial condition (see eq. S2). We further imposed the constraint that, once the speed reaches zero, it remains zero for all subsequent times (see solid lines in Fig. 4C). In this formulation, t is the independent variable and v_t is the dependent variable, while the four parameters free to vary in the fit are K, τ, $v_{t,start}$, and $v_{t,target}$. To estimate these parameters, we fitted the model to the experimental data using nonlinear least-squares minimization implemented in the Python library LMFIT (*50*). For the speed traces corresponding to continuous swimming, the best fit estimates of $v_{t,target}$ matched the values to which v_t converged after the initial transient. The range of $v_{t,target}$ obtained in the continuous case was then used to constrain the fitting procedure for the speed traces corresponding to intermittent swimming. Accordingly, in the fitting procedure, we restricted $v_{t,target}$ to the range [2, 6] cm/s. In addition, to ensure meaningful fits, we constrained the delay τ to the interval [0.05,0.5] s. Using the inferred parameters, we computed the gain-delay product $K\tau$ and the speed ratio $v_{t,start}/v_{t,target}$ to locate each fish within the dynamical phase space (Fig. 4B).

Manipulation of sensory feedback

Vestibular: High-viscosity medium

Water viscosity was increased using dextran (Sigma-Aldrich; molecular weight, 450 to 650 kDa), prepared as an 8% (w/v) solution in water (*51*). Viscosity was measured with a rheometer (Anton Paar), showing a 10-fold increase compared to water at the same experimental temperature. The preparation and measurement were repeated three times, yielding consistent results. We chose to increase medium viscosity 10-fold to match the nearly 10-fold rise in Reynolds number observed from 2- to 5-week-old fish. This manipulation allowed us to artificially reverse the transition by mimicking the hydrodynamic changes experienced during development. To avoid filling the entire 40 cm–by–40 cm arena with the viscous medium, these experiments were conducted in a smaller arena (7 cm–by–7 cm). This was not a limitation, as fish swam more slowly and took longer to reach the arena boundaries in the viscous medium, and the aim of the experiment was simply to assess whether swimming was continuous or intermittent. Moreover, because of reduced visibility of tail motion in the viscous medium, we could only extract the fish speed v_f, not the tail speed v_t. Each fish was first recorded in normal water, then in the viscous medium (where it remained for a maximum of 15 min), and lastly again in normal water as a control.

Lateral line: Ablation

The lateral line of 4-week-old *Danionella* was chemically ablated with neomycin, following a protocol established in zebrafish larvae (*52*) and previously validated in adult *Danionella* (*17*). Specifically, fish were immersed in a 200 μM neomycin (Sigma-Aldrich) solution for 30 min and then thoroughly rinsed in Ringer solution. Ringer solution was used to match blood osmotic pressure, which helped preserve cell integrity and function at the ablation site. The fish was then allowed

to recover for 1 hour in the incubator. All experiments were carried out within 5 hours of the lateral line ablation to prevent neuromast regeneration.

Following Veith *et al.* (*17*), ablation was confirmed by exposing treated *Danionella* to a 50 μM solution of 4-Di-2-ASP (Sigma-Aldrich) for 5 min, followed by fluorescence imaging using a binocular microscope (see fig. S11D). The 4-Di-2-ASP bulk solution was prepared in E3 medium with 1% ethanol to aid dissolution.

Visual: Complete darkness experiments

Experiments were conducted in complete darkness to deprive the fish of any visual cues: The projector was turned off, and the enclosure surrounding the entire setup was internally lined with black sheets and fully closed.

Virtual reality experiments

The experiments were conducted in a virtual environment as described in Demarchi *et al.* (*15*). The fish were presented with visual currents in the forward direction with an optic flow rate $\omega_{ext} = 0.5$ rad/s, lasting for 30 s, and separated by pauses of 30 s. We probed five different values of the feedback gain (the scaling factor α between fictive fish speed V and feedback optic flow rate), corresponding to five different target speeds $V_{target} = \omega_{ext} / \alpha$ for which the fish stabilizes its position in the virtual environment. Each target speed was presented in two distinct trials in a randomized fashion. To reduce the potential bias due to struggling movements, which are frequent in head-tethered configurations, the average bout duration per trial was computed as the expected duration of a swimming event selected by picking at random a time where the fish was swimming.

Supplementary Materials

The PDF file includes:

Supplementary Text
Table 1
Figs. S1 to S13
Legends for movies S1 to S7
References

Other Supplementary Material for this manuscript includes the following:

Movies S1 to S7

REFERENCES

1. K. Hashikawa, Y. Hashikawa, B. Briones, K. Ishii, Y. Liu, M. A. Rossi, M. L. Basiri, J. Y. Chen, O. R. Ahmad, R. V. Mukundan, N. L. Johnston, R. C. Simon, J. C. Soetedjo, J. R. Siputro, J. A. McHenry, R. D. Palmiter, D. R. Rubinow, L. S. Zweifel, G. D. Stuber, Esr1-dependent signaling and transcriptional maturation in the medial preoptic area of the hypothalamus shapes the development of mating behavior during adolescence. bioRxiv 640339 [Preprint] (2025). https://doi.org/10.1101/2025.02.26.640339.
2. M. Fernandez-Acosta, R. Zanini, F. Heredia, Y. A. Volonté, J. Menezes, K. Prüger, J. Ibarra, M. Arana, M. S. Pérez, J. A. Veenstra, C. Wegener, A. M. Gontijo, A. Garelli, Triggering and modulation of a complex behavior by a single peptidergic command neuron in *Drosophila*. *Proc. Natl. Acad. Sci.* **122**, (2025).
3. O. Fehér, H. Wang, S. Saar, P. P. Mitra, O. Tchernichovski, De novo establishment of wild-type song culture in the zebra finch. *Nature* **459**, 564–568 (2009).
4. M. A. R. Koehl, When does morphology matter? *Annu. Rev. Ecol. Evol. Syst.* **27**, 501–542 (1996).
5. M. H. Dickinson, C. T. Farley, R. J. Full, M. A. R. Koehl, R. Kram, S. Lehman, How animals move: An integrative view. *Science* **288**, 100–106 (2000).
6. F. J. Diedrich, W. H. Warren, Why change gaits? Dynamics of the walk-run transition. *J. Exp. Psychol. Hum. Percept. Perform.* **21**, 183–202 (1995).
7. F. J. Diedrich, W. H. Warren, The dynamics of gait transitions: Effects of grade and load. *J. Mot. Behav.* **30**, 60–78 (1998).
8. C. T. Farley, C. R. Taylor, A mechanical trigger for the trot-gallop transition in horses. *Science* **253**, 306–308 (1991).
9. D. Owaki, A. Ishiguro, A quadruped robot exhibiting spontaneous gait transitions from walking to trotting to galloping. *Sci. Rep.* **7**, 277 (2017).
10. L. Schulze, J. Henninger, M. Kadobianskyi, T. Chaigne, A. I. Faustino, N. Hakiy, S. Albadri, M. Schuelke, L. Maler, F. del Bene, B. Judkewitz, Transparent Danionella translucida as a genetically tractable vertebrate brain model. *Nat. Methods* **15**, 977–983 (2018).
11. R. Britz, K. W. Conway, L. Rüber, The emerging vertebrate model species for neurophysiological studies is Danionella *cerebrum*, new species (Teleostei: Cyprinidae). *Sci. Rep.* **11**, 18942 (2021).
12. D. Zada, L. Schulze, J.-H. Yu, P. Tarabishi, J. L. Napoli, M. Lovett-Barron, Development of neural circuits for social motion perception in schooling fish. bioRxiv 563839 [Preprint] (2023). https://doi.org/10.1101/2023.10.25.563839.
13. M. Hoffmann, J. Henninger, J. Veith, L. Richter, B. Judkewitz, Blazed oblique plane microscopy reveals scale-invariant inference of brain-wide population activity. *Nat. Commun.* **14**, 8019 (2023).
14. K. E. Fouke, Z. He, M. D. Loring, E. A. Naumann, Neural circuits underlying divergent visuomotor strategies of zebrafish and Danionella cerebrum. *Curr. Biol.* **35**, 2457–2466.e4 (2025).
15. L. Demarchi, M. Coraggioso, A. Hubert, T. Panier, G. Morvan-Dubois, V. Bormuth, G. Debrégeas, Logarithmic coding leads to adaptive stabilization in the presence of sensorimotor delays. *Proc. Natl. Acad. Sci. U.S.A.* , e2510385122 (2025).
16. A. H. Groneberg, L. E. Dressler, M. Kadobianskyi, J. Müller, B. Judkewitz, Development of sound production in *Danionella cerebrum*. *J. Exp. Biol.* **227**, jeb247782 (2024).
17. J. Veith, T. Chaigne, A. Svanidze, L. E. Dressler, M. Hoffmann, B. Gerhardt, B. Judkewitz, The mechanism for directional hearing in fish. *Nature* **631**, 118–124 (2024).
18. V. A. N. O. Cook, A. H. Groneberg, M. Hoffmann, M. Kadobianskyi, J. Veith, L. Schulze, J. Henninger, R. Britz, B. Judkewitz, Ultrafast sound production mechanism in one of the smallest vertebrates. *Proc. Natl. Acad. Sci. U.S.A.* **121**, e2314017121 (2024).
19. M. J. Lighthill, Large-amplitude elongated-body theory of fish locomotion. *Proc. Biol. Sci.* **179**, 125–138 (1971).
20. D. Weihs, Energetic advantages of burst swimming of fish. *J. Theor. Biol.* **48**, 215–229 (1974).
21. T. Darveniza, R. Wong, S. I. Zhu, Z. Pujic, B. Sun, M. Levendosky, R. Agarwal, M. H. McCullough, G. J. Goodhill, Larval zebrafish minimize energy consumption during hunting via adaptive movement selection. *Proc. Natl. Acad. Sci. U.S.A.* **123**, e2513853123 (2026).
22. G. Li, D. Kolomenskiy, H. Liu, R. Godoy-Diana, B. Thiria, Intermittent versus continuous swimming: An optimization tale. *Phys. Rev. Fluids* **8**, 013101 (2023).
23. M. Gazzola, M. Argentina, L. Mahadevan, Scaling macroscopic aquatic locomotion. *Nat. Phys.* **10**, 758–761 (2014).
24. J. L. Van Leeuwen, T. Van Der Meulen, H. Schipper, S. Kranenbarg, A functional analysis of myotomal muscle-fibre reorientation in developing zebrafish *Danio rerio*. *J. Exp. Biol.* **211**, 1289–1304 (2008).
25. A. B. Saleem, A. Ayaz, K. J. Jeffery, K. D. Harris, M. Carandini, Integration of visual motion and locomotion in mouse visual cortex. *Nat. Neurosci.* **16**, 1864–1869 (2013).
26. M. S. Creamer, O. Mano, D. A. Clark, Visual control of walking speed in Drosophila. *Neuron* **100**, 1460–1473.e6 (2018).
27. U. K. Müller, J. L. V. Leeuwen, S. V. Duin, H. Liu, An un-momentous start to life: Can hydrodynamics explain why fish larvae change swimming style? *J. Biomech. Sci. Eng.* **4**, 37–53 (2009).
28. J. J. Videler, D. Weihs, Energetic advantages of burst-and-coast swimming of fish at high speeds. *J. Exp. Biol.* **97** (1): 169–178 (1982).
29. G. Rajan, J. Lafaye, G. Faini, M. Carbo-Tano, K. Duroure, D. Tanese, T. Panier, R. Candelier, J. Henninger, R. Britz, B. Judkewitz, C. Gebhardt, V. Emiliani, G. Debregeas, C. Wyart, F. del Bene, Evolutionary divergence of locomotion in two related vertebrate species. *Cell Rep.* **38**, 110585 (2022).
30. E. J. Denton, J. A. B. Gray, Stimulation of the acoustico-lateralis system of clupeid fish by external sources and their own movements. *Philos. Trans. R Soc. Lond. B Biol. Sci.* **341**, 113–127 (1993).
31. T. A. Delomas, K. Dabrowski, Larval rearing of zebrafish at suboptimal temperatures. *J. Therm. Biol.* **74**, 170–173 (2018).
32. N. M. Duff, R. E. Sommerfeld, M. K. Litvak, Discriminating sex in zebrafish (*Danio rerio*) using geometric morphometrics. *Zebrafish* **16**, 207–213 (2019).
33. K. E. Severi, R. Portugues, J. C. Marques, D. M. O'Malley, M. B. Orger, F. Engert, Neural control and modulation of swimming speed in the larval zebrafish. *Neuron* **83**, 692–707 (2014).
34. T. Thiele, J. Donovan, H. Baier, Descending control of swim posture by a midbrain nucleus in zebrafish. *Neuron* **83**, 679–691 (2014).
35. D. Weihs, Energetic significance of changes in swimming modes during growth of larval anchovy. Fishery Bulletin: vol. 77, no. 3, (1980).
36. Y. Isoe, Y. F. Mabene, M. Bind, F. Engert, Divergent spatiotemporal integration of whole-field visual motion in medaka and zebrafish. bioRxiv 671687 [Preprint] (2025). https://doi.org/10.1101/2025.08.22.671687.
37. D. S. Mearns, S. A. Hunt, M. W. Schneider, A. V. Parker, M. Stemmer, H. Baier, Diverse prey capture strategies in teleost larvae. *eLife* **13**, RP98347 (2025).

38. R. Portugues, F. Engert, Adaptive locomotor behavior in larval zebrafish. *Front. Syst. Neurosci.* **5**, 72 (2011).
39. M. B. Ahrens, J. M. Li, M. B. Orger, D. N. Robson, A. F. Schier, F. Engert, R. Portugues, Brain-wide neuronal dynamics during motor adaptation in zebrafish. *Nature* **485**, 471–477 (2012).
40. P. Ramdya, A. J. Ijspeert, The neuromechanics of animal locomotion: From biology to robotics and back. *Sci. Robot.* **8**, eadg0279 (2023).
41. J. Redmon, S. Divvala, R. Girshick, A. Farhadi, You Only Look Once: Unified, Real-Time Object Detection, IEEE Conference on Computer Vision and Pattern Recognition (CVPR), Las Vegas, NV, USA, pp. 779–788 (2016).
42. R. E. Johnson, S. Linderman, T. Panier, C. L. Wee, E. Song, K. J. Herrera, A. Miller, F. Engert, Probabilistic models of larval zebrafish behavior reveal structure on many scales. *Curr. Biol.* **30**, 70–82.e4 (2020).
43. T. D. Pereira, N. Tabris, A. Matsliah, D. M. Turner, J. Li, S. Ravindranath, E. S. Papadoyannis, E. Normand, D. S. Deutsch, Z. Y. Wang, G. C. McKenzie-Smith, C. C. Mitelut, M. D. Castro, J. D'Uva, M. Kislin, D. H. Sanes, S. D. Kocher, S. S. H. Wang, A. L. Falkner, J. W. Shaevitz, M. Murthy, SLEAP: A deep learning system for multi-animal pose tracking. *Nat. Methods* **19**, 486–495 (2022).
44. V. Štih, L. Petrucco, A. M. Kist, R. Portugues, Stytra: An open-source, integrated system for stimulation, tracking and closed-loop behavioral experiments. *PLoS Comput. Biol.* **15**, e1006699 (2019).
45. M. J. McHenry, E. Azizi, J. A. Strother, The hydrodynamics of locomotion at intermediate Reynolds numbers:undulatory swimming in ascidian larvae (*Botrylloides*sp.). *J. Exp. Biol.* **206**, 327–343 (2003).
46. A. P. S. Bhalla, R. Bale, B. E. Griffith, N. A. Patankar, A unified mathematical framework and an adaptive numerical method for fluid-structure interaction with rigid, deforming, and elastic bodies. *J. Comput. Phys.* **250**, 446–476 (2013).
47. G. Guennebaud, B. Jacob, *et al.*, Eigen v3, http://eigen.tuxfamily.org (2010).
48. H. Childs, E. Brugger, B. Whitlock, J. Meredith, S. Ahern, D. Pugmire, K. Biagas, M. Miller, C. Harrison, G. H. Weber, H. Krishnan, T. Fogal, A. Sanderson, C. Garth, E. Wes Bethel, D. Camp, O. Rubel, M. Durant, J. Favre, Paul Navratil, "VisIt: An end-user tool for visualizing and analyzing very large data," in *High Performance Visualization: Enabling Extreme-Scale Scientific Insight*,Chapman & Hall/CRC, ed. 1, 358–373 (2012).
49. K. Tainaka, T. C. Murakami, E. A. Susaki, C. Shimizu, R. Saito, K. Takahashi, A. Hayashi-Takagi, H. Sekiya, Y. Arima, S. Nojima, M. Ikemura, T. Ushiku, Y. Shimizu, M. Murakami, K. F. Tanaka, M. Iino, H. Kasai, T. Sasaoka, K. Kobayashi, K. Miyazono, E. Morii, T. Isa, M. Fukayama, A. Kakita, H. R. Ueda, Chemical landscape for tissue clearing based on hydrophilic reagents. *Cell Rep.* **24**, 2196–2210.e9 (2018).
50. M. Newville, R. Otten, A. Nelson, T. Stensitzki, A. Ingargiola, D. Allan, A. Fox, F. Carter, M. Rawlik, LMFIT: Non-linear least-squares minimization and curve-fitting for Python (2025).
51. F. Carrasco, E. Chornet, R. P. Overend, J. Costa, A generalized correlation for the viscosity of dextrans in aqueous solutions as a function of temperature, concentration, and molecular weight at low shear rates. *J. Appl. Polym. Sci.* **37**, 2087–2098 (1989).
52. J. A. Harris, A. G. Cheng, L. L. Cunningham, G. MacDonald, D. W. Raible, E. W. Rubel, Neomycin-induced hair cell death and rapid regeneration in the lateral line of zebrafish (Danio rerio). *J. Assoc. Res. Otolaryngol.* **4**, 219–234 (2003).
53. H. Smith, "An introduction to delay differential equations with applications to the life sciences, vol. 57 of texts," in *Applied Mathematics*,Springer New York, 13–14 (2011).
54. M. Westerfield, *The Zebrafish Book. A guide for the Laboratory Use of Zebrafish (Danio rerio)*, Zebrafish International Resource Center, ed. 4, (2000).

Acknowledgments: We thank the members of the IBPS aquatic animal facility for assistance in animal care and D. Demirdelen for help with egg collection and larval rearing. We are grateful to B. Judkewitz and F. Del Bene for sharing their *Danionella* lines and to J. Lafaye for helping setting up the *Danionella* facility. We also thank R. Portugues for valuable discussions and M. Dommanget-Kott for support with debugging. **Funding:** The Laboratoire Jean Perrin acknowledge the support, for this work, of the European Union's Horizon 2020 research and innovation programme under the Marie Sklodowska-Curie grant agreement no. 860949 and by the ANR Locomat project (ANR-21-CE16-0037). **Author contributions:** Conceptualization: M.C., G.D., L.D., and V.B. Data curation: M.C. Formal analysis: M.C. and L.D. Funding acquisition: V.B. and G.D. Investigation: M.C., L.D., and R.W. Methodology: M.C., L.D., R.W., V.D., C.C., T.P., G.M.-D., G.J.G., V.B., and G.D. Project administration: G.D. and V.B. Resources: G.M.-D., V.B., and G.D. Software: M.C., V.D., R.W., L.D., and T.P. Supervision: G.D. Validation: M.C. Visualization: M.C., L.D., and R.W. Writing—original draft: M.C. Writing—review and editing: M.C., G.D., L.D., V.B., R.W., and G.J.G. **Competing interests:** The authors declare that they have no competing interests. **Data, code, and materials availability:** Data and code are available on Zenodo: https://doi.org/10.5281/zenodo.17650136. All data and code needed to evaluate and reproduce the results in the paper are present in the paper and/or the Supplementary Materials. These experiments did not generate any new materials.

Submitted 29 September 2025
Accepted 20 March 2026
Published 22 April 2026
10.1126/sciadv.aec6922

Science Advances

A sensorimotor instability drives a locomotor transition during fish development

Monica Coraggioso, Leonardo Demarchi, Robert Wong, Vito Dichio, Chloé Chaumeton, Thomas Panier, Ghislaine Morvan-Dubois, Geoffrey J. Goodhill, Volker Bormuth, and Georges Debrégeas

Sci. Adv. **12** (17), eaec6922. DOI: 10.1126/sciadv.aec6922